

Numerical study on the moment capacity of zed-section purlins under uplift loading

Jue Zhu^{1,*}, Jian-kang Chen¹, Chong Ren²

¹*Faculty of Mechanical Engineering and Mechanics, Ningbo University, Ningbo, China*

²*School of Civil Engineering, University of Birmingham, Birmingham, UK*

ABSTRACT

In this paper a nonlinear finite element analysis model is established for cold-formed steel zed-section purlins subjected to uplift loading. In the model, the lateral and rotational restraints provided by the sheeting to the purlin are simplified as a lateral rigid restraint imposed at the upper flange-web junction and a rotational spring restraint applied at the mid of the upper flange where the sheeting is fixed. The analyses are performed by considering both geometrical and material nonlinearities. The influences of the rotational spring stiffness and initial geometrical imperfections on the uplift loading capacity of the purlin are investigated numerically. It is found that the rotational spring stiffness has significant influence on the purlin performance. However, the influence of the initial geometric imperfections on the purlin performance is found only in purlins of medium or long length with no or low rotational spring stiffness.

Keywords: zed-purlin, uplift, imperfection, nonlinear analysis, lateral-torsional buckling, moment capacity, finite element.

1. INTRODUCTION

Cold-formed steel sections such as zed, channel and sigma sections are widely used in buildings as purlins and rails to support the corrugated sheeting. In practice, they are usually connected to the sheeting by screwing through the crest of the corrugated sheeting and purlin flange (Rhodes 1992; ENV1993-1-3 2006). The corrugated sheeting attached to the purlin provides two main restraining effects to resist

* Corresponding author. Assistant Professor, Ph.D. E-mail: zhujue@nbu.edu.cn

Note: Copied from the manuscript submitted to "Structural Engineering and Mechanics, An International Journal" for presentation at ASEM13 Congress

the lateral and rotational displacements (ENV1993-1-3 2006). For most types of sheeting, the sheeting membrane stiffness provides sufficiently lateral restraint and therefore the lateral displacement at the upper flange-web junction may be assumed to be fully restrained (ENV1993-1-3 2006; Li 2007). The rotational stiffness comes from both the rotational stiffness of the sheeting itself and that of the purlin-sheeting connection, which depends on a number of factors including the type of sheeting, the type and dimensions of the purlin, and the spacing of fixings between the sheeting and purlin. The restraining of sheeting to purlin has significant influence on purlin performance. For example, under downward loading the lateral restraint can prevent the purlin from lateral-torsional buckling since the flange in compression is laterally restrained by the sheeting (ENV1993-1-3 2006; Li 2010). Under uplift loading, however, the restrained flange is in tension and the free flange is in compression, so that the free flange can still have a lateral-torsional buckling (ENV1993-1-3 2006).

In literature, there have been a numerous studies on the effects of sheeting on the bending and buckling behavior of purlins (Vrany 2006; Vieira 2010). Ye et al. studied the influence of sheeting on the linear bending of roof purlins using analytical methods (Ye 2004). Later, they also investigated the influence of sheeting on the local and distortional buckling behaviour of roof purlins using finite strip analysis methods (Ye 2002). Lucas et al. studied the interaction between the sheeting and purlins using finite element methods (Lucas 1997). The lateral-torsional buckling of purlins subjected to downward and/or upward loads were also discussed by several researchers (Li 2004; Toma 1994; Roger 1997; Svensson 1985; Sokol 1996). Analytical models were developed to predict the critical loads of lateral-torsional buckling and the influence of sheeting on the lateral-torsional buckling behaviour of roof purlins (Svensson 1985; Sokol 1996; Peköz 1982). Experimental tests were performed on both bridged and unbridged zed- and channel-section purlins under uplift loads (Hancock 1990; Rousch 1997). Calculation models for predicting the rotational restraint stiffness of the sheeting were proposed (Katnam 2007; Katnam 2007). Design rules have been developed specially for the case where the free flange of the purlin is in compression (Vieira 2010). Recently, Li et al. proposed an analytical model for calculating the linear bending stresses in roof purlins from which the influence of sheeting on the bending performance of the roof purlin can be evaluated (Li 2012; Ren 2012).

Most of the works mentioned above are the linear analysis. For ultimate state analysis, nonlinear analysis is needed. For thin-walled structures this should include both geometrical and material nonlinearities. In this paper, a nonlinear finite element analysis model is established for cold-formed steel zed-section purlins subjected to uplift loading. In the model, the lateral and rotational restraints provided by the sheeting to the purlin are simplified as a lateral rigid restraint imposed at the upper flange-web junction and a rotational spring restraint applied at the mid of the upper flange where the sheeting is fixed. The analyses are performed by considering both geometrical and material nonlinearities. The influence of initial geometrical imperfections on the uplift loading capacity of the purlin is also investigated numerically.

2. FINITE ELEMENT ANALYSIS MODEL

Consider a zed-purlin-sheeting system subjected to an uplift load, in which the

upper flange of the zed-section is connected to the sheeting by self-drilling/tapping screw fasteners. The attached sheeting provides lateral and rotational restraints to the section, which are simplified as a lateral rigid restraint imposed at the upper flange-web junction and a rotational spring restraint applied at the mid of the upper flange where the sheeting is fixed, as shown in Figure 1. The dimensions of the zed-section analyzed are, web depth $h = 120$ mm, flange width $b = 50$ mm, lip length $c = 15$ mm, and thickness $t = 1.5$ mm. The material properties of the zed-section are, Young's modulus $E = 210$ GPa, Poisson's ratio $\mu = 0.3$, yield stress $\sigma_y = 350$ MPa, and density $\rho = 7850$ kg/m³. The stress-strain curve used for the zed-section is assumed to follow that of the elastic-perfectly plastic material. The analyses are carried out for three different rotational stiffness values ($k = 0$, $k = 300$ N/rad and $k = 750$ N/rad) in seven different lengths ranging from $L = 4000$ mm to $L = 10000$ mm. For why $k = 300$ N/rad and 750 N/rad are chosen is because those were based on tow extreme cases of the practically used cladding.

The purlin is assumed to be simply supported on its both ends and subjected to a uniformly distributed uplift load acting on the middle line of the upper flange. Due to symmetry, only half length of the purlin is modeled. The displacement boundary conditions on the simply supported cross-section are only applied to the web line at which the lateral and vertical components of the displacement are assumed to be zero (i.e. $v = w = 0$). This is to match the cleat connection used in practice. The displacement boundary conditions on the symmetric cross-section are applied to all lines in which the longitudinal component of the displacement and the angles rotated about the vertical and lateral axes are assumed to be zero (i.e. $u_x = \phi_y = \phi_z = 0$). The lateral rigid restraint imposed at the upper flange-web junction is modeled by adding a zero lateral displacement boundary condition on the line representing the upper flange-web junction.

The analyses are conducted using the finite element analysis software ANSYS. The four-node shell element SHELL143 is employed, which has six degrees of freedom at each node. The element has plasticity, creep, stress stiffening, large deflection and small strain capabilities. In addition, a two-node spring-damper element COMBIN14 is also employed to describe the rotational spring restraint applied at the middle line of the upper flange where the uplift load is also applied. The spring-damper element has longitudinal or torsional capacity in 1-D, 2-D and 3-D applications and is able to represent the spring restraint boundary conditions. In order to ensure that the results obtained are accurate, meshes of different element sizes were used first and it was found that the meshes of element sizes smaller than 10 mm provided almost no difference in results. Therefore, all analyses have been kept to have a maximum element size of 10 mm. Figure 2 shows a typical element mesh and corresponding boundary conditions used in the analyses. All analyses are performed by taking into account both geometrical and material nonlinearities using an arc-length algorithm.

3. FINITE ELEMENT ANALYSIS WITHOUT CONSIDERING INITIAL GEOMETRIC IMPERFECTIONS

For given purlin length and rotational spring stiffness, one can obtain the load-displacement curve from the finite element analysis. Figure 3 shows the load-displacement curves of the purlin of length $L = 4000$ mm for three different rotational spring stiffness values, in which the load is the uniformly distributed uplift load acting on the middle line of the upper flange and the displacements are the vertical displacement at the upper flange-web junction and the horizontal displacement at the lower flange-web junction, both on the symmetric section of the purlin. It can be seen from the figure that, the load-displacement curves for purlin with $k = 0$ are different from those for purlin with $k = 300$ N/rad or $k = 750$ N/rad. In the former, the load increases with the displacements until the load nears its up-limit value where a small increase in the load results in a rapid increase in displacements. This indicates that the failure of the purlin is a typical limiting failure of plasticity. In the latter, the load increases with the displacements until it reaches to a peak point. After the peak point, the load decreases with further increased displacements, indicating that the failure of the purlin is a typical buckling failure. As it is to be expected, the failure load of the purlin increases with the rotational spring stiffness. For example, the failure load of the purlin with $k = 750$ N/rad is over twice that of the purlin with $k = 0$.

The reason that the rotational spring not only increases the failure load but also alters the failure type of the purlin is because the rotational spring provides some restraints on the purlin's pre-buckling twisting displacements. When a beam is subjected to a transverse load, it is initially bent about its major axis. However, after the beam occurs a lateral-torsional buckling, the bending axis suddenly moves from its major axis to minor axis. Therefore, the post-buckling curve is usually unstable, like what is shown in Figure 3 for the purlins with $k = 300$ N/rad and $k = 750$ N/rad. However, if a beam is initially bent about its minor axis or is simultaneously subjected to bending and twisting, the beam deforms gradually towards its post-buckling mode and will eventually have a plastic failure, like what is shown in Figure 3 for the purlin with $k = 0$.

Figure 4 shows the deformed shapes of the purlins with three different k values when the loads reach their ultimate values. It can be seen from the figure that, when $k = 0$ the purlin has severe twisting deformation, which significantly reduces the flexural rigidity in the loading direction but increases the flexural rigidity in the perpendicular direction. As a consequence of this, the bending stresses increase much quicker than the actual load does. This leads the purlin eventually to have a plastic failure. The deformations of the purlins with $k = 300$ N/rad and $k = 750$ N/rad are very similar; both are small when compared to that of the purlin with $k = 0$.

Figure 5 shows the load-displacement curves of the purlin of length $L = 7000$ mm for three different rotational spring stiffness values. It is found from the figure that the curves for $k = 300$ N/rad and $k = 750$ N/rad are very similar to those shown in Figure 3, except that the loads are smaller as the purlin is longer. The case for $k = 0$, however, is very interesting. It is observed from Figure 5 that the load-displacement curves corresponding to $k = 0$ can be divided into three different regions. The first one is the

initial part of the curves where both displacements increase somehow linearly with the load. The second one is the mid part of the curves where both displacements increase rapidly while the load increases very slowly. The third one is the last part of the curves where the vertical displacement increases with the load until it reaches to the maximum load point, while the horizontal displacement does not increase very much with the increased load. In order to discover why there exists a flat part in the mid of the load-displacement curves, the linear buckling analysis is also carried out, which shows the purlin has a lateral-torsional buckling critical load of 0.13 kN/m. This critical load matches very well with the load in the mid part of the curves. This indicates that the purlin, which is bent initially about its major axis, has had a lateral-torsional buckling when the load reaches about 0.13 kN/m. After the buckling the purlin is bent about its minor axis. However, since the plastic bending load about the minor axis is greater than the critical buckling load 0.13 kN/m, the load can increase continuously until the purlin becomes fully plastic. Therefore, the final failure of the purlin is characterized by the plastic bending failure. Figure 6 shows the deformed shapes of the purlins when the loads reach to their ultimate values. Again, the deformed shapes are very similar, although the longitudinal stress contours are different. It should be pointed out that, though the plastic failure load of the purlin with $k = 0$ is more than twice its critical buckling load, the purlin develops large vertical and horizontal deflections while it buckles. Therefore, in terms of the serviceability the purlin will fail when the lateral-torsional buckling occurs even though the post-lateral-torsional buckling is actually stable.

Figure 7 shows the load-displacement curves of the purlin of length $L = 10000$ mm for three different rotational spring stiffness values. The corresponding deformed shapes of the purlins when the loads reach to their ultimate values are shown in Figure 8, respectively. The main features of these figures are similar to those shown in Figures 5 and 6 and thus are not discussed further. To demonstrate the difference between the critical load of lateral-torsional buckling calculated from linear buckling analysis and the failure load obtained from the nonlinear analysis, Table 1 provides a detailing comparison. For purlins with $k = 300$ N/rad or $k = 750$ N/rad, the critical buckling load is found to be higher than the plastic failure load. This is partly due to the influence of geometrical nonlinearity and partly due to the influence of material nonlinearity before the buckling occurs. For short length purlins without rotational spring restraint, the critical buckling load is higher than the plastic failure load, whereas for medium and long length purlins, the critical buckling load is lower than the plastic failure load. This implies that the influence of the rotational spring on the failure mode of the purlin is also dependent on the purlin length.

4. FINITE ELEMENT ANALYSIS WITH CONSIDERING INITIAL GEOMETRIC IMPERFECTIONS

The analyses described above did not consider the initial geometric imperfections. In practice due to transport and construction purlins have more or less some geometric imperfections. These geometric imperfections may have influence on the performance as well as the failure mode of the purlin. In this section finite element analyses are presented, which consider the initial geometric imperfections produced by purlin self-weight. To take account the initial geometric imperfections, each run involves two steps. The first step is to obtain the initial geometric imperfections, for which a linear analysis is conducted. Figure 9 shows a typical geometric imperfection of a purlin with vertical and lateral displacement contours. The second step is to obtain the load-displacement curves of the purlin under the uplift loading, which is done by taking into account both geometrical and material nonlinearities using an arc-length algorithm as described in the preceding section.

Figure 10 shows the load-displacement curves of the imperfection purlin of length $L = 4000$ mm for three different rotational spring stiffness values. Comparing Figure 10 with Figure 3, almost no difference can be found. The reason for this is because for a short length purlin, the deflections generated by the purlin self-weight are rather small. Hence, the initial geometric imperfections have almost no influence on the load-displacement curves. This is also demonstrated by the deformed shapes plotted in Figure 11. As the purlin length increases, the deflections of the purlin due to its self-weight also increase. Figure 12 shows the load-displacement curves of the imperfect purlin of length $L = 7000$ mm for three different rotational spring stiffness values. Interestingly, the load-displacement curves for $k = 300$ N/rad and $k = 750$ N/rad are found to be almost the same as those shown in Figure 5. However, the load-displacement curve for $k = 0$ is found quite different from that shown in Figure 5, not only in terms of the failure load but also in terms of the curve shape in which the horizontal displacement is actually deformed in an opposite direction. When the initial geometric imperfection is taken into account, the purlin is failed by a lateral-torsional buckling, instead of the plastic failure found in the perfect purlin. The critical load is found to be greater than the critical load but lower than the failure load of the corresponding perfect purlin. The reason for this is because the initial deformation of the imperfect purlin, which is not favorable to the lateral-torsional buckling. Figure 13 shows the deformed shapes of the imperfect purlins, which shows that the purlin of $k = 0$ has a severe twisting deformation, whereas the purlin of $k = 300$ N/rad or $k = 750$ N/rad has a very similar deformed shape as that shown in Figure 6. This indicates that with the increase of the purlin length, the initial geometric imperfections may have important influence on the purlin performance and failure mode if the rotational restraint is not strong enough. This is further demonstrated by the results shown in Figures 14 and 15 for the purlin with a length of 1000 mm, showing that the failure load and failure mode of the purlin with $k = 0$ are quite different from those shown in Figures 7 and 8,

respectively.

Figure 16 shows a comparison of the failure loads of the purlins with and without considering the initial geometric imperfections. It can be seen from the figure that the failure load in all cases decreases with the increase of purlin length. Also, it can be seen from the figure that the influence of the initial geometric imperfections on the failure load increases with the purlin length but decreases with increased rotational spring stiffness. In the practical design, one is more interested in the moment capacity rather than the failure load. Figure 17 shows the variation of the moment capacity of the purlin with its length, in which the moment capacity is calculated directly based on the failure load and purlin length using the simple formula for beams, i.e. $M = qL^2/8$. Interestingly, when the load is plotted using its moment, it is found the failure moment does not change very much with the purlin length for the perfect beams. This indicates that the failure moment of a purlin subjected to an uplift load is almost independent of its length. When the initial geometric imperfection is taken into account, however, the failure moment of the purlin with no rotational spring restraint still decreases with the increase of the purlin length.

5. VALIDATION OF THE MODEL

The present nonlinear finite element model is validated using the experimental data reported in (Hancock 1990; Rousch 1997), in which the dimensions of the zed-section purlin analyzed are web depth $h = 202.8$ mm, upper flange width $b_1 = 80.7$ mm, lower flange width $b_2 = 72.5$ mm, lip length $c = 21.5$ mm, and thickness $t = 1.5$ mm. The material properties are Young's modulus $E = 200$ GPa, Poisson's ratio $\mu = 0.3$, and yield stress $\sigma_y = 450$ MPa. The torsion restraint provided by the sheeting is taken as 0.023 N/mm², as provided in (Hancock 1990; Rousch 1997). The loading condition and boundary conditions employed are exactly the same as those used in preceding sections. Figure 18 shows the comparisons of the finite element analysis and experimental measurement results. It can be seen from the figure that, for the lateral displacement at the lower flange-web junction the finite element analysis results compare closely with those obtained in the test. However, for the vertical displacement at the upper flange-web junction the finite element analysis results are a little higher than those obtained in tests. This is probably due to the influence of the sheeting bending stiffness, which is not taken into account in the FEA model, but in the test it may take some loading. Nevertheless, in overall, the FEA predictions agree well with the test data. This indicates that the idealized boundary conditions proposed in the present study are able to represent the standard two-hole cleat support conditions used in practice.

6. CONCLUSIONS

This paper has presented a numerical investigation on the influence of the rotational spring stiffness and initial geometric imperfections on the performance of cold-formed steel purlins under the action of uplift loading using nonlinear finite element analysis methods. From the results obtained, the following conclusions can be drawn.

The rotational spring stiffness has significant influence on the performance of the purlin. Not only can it increase the failure load but also can change the failure mode of the purlin.

For the purlin with strong rotational spring restraint, the failure of the purlin is mainly controlled by the buckling. However, due to the influence of the deformations and material yielding prior to the buckling, the failure load is generally less than the critical load obtained directly from the linear buckling analysis.

For the perfect purlin with no rotational restraint, the failure of the purlin is mainly due to the plastic bending failure occurring in the plane of minor axis. However before the failure, the purlin undergoes a lateral-torsional buckling.

The initial geometric imperfections produced by purlin self-weight have significant influence on the performance of medium and long length purlins with no or low rotational spring stiffness. The initial geometric imperfection not only reduces the failure load but also changes the failure mode of the purlin from a plastic failure to a lateral-torsional buckling failure. However, for short length purlins or purlins with strong rotational spring restraint the influence of the initial geometric imperfections on the purlin performance can generally be ignored.

The failure load of the purlin decreases with the increase of purlin length. However, the failure moment calculated from the failure load is almost independent of the purlin length if the initial geometric imperfections can be ignored.

The comparison of the finite element analysis and experimental measurement results has demonstrated that the idealized boundary conditions proposed in the present study are able to represent the standard two-hole cleat support conditions used in practice.

ACKNOWLEDGEMENT

The first two authors would like to acknowledge the supports received from the COE Program of Zhejiang Provincial Government at Ningbo University (Grant No. zj1004), the Natural Science Foundation of Zhejiang Province (No.Y13A020027), Ningbo Municipal Natural Science Foundation (No. 2012A610162) and K.C. Wong Magna Fund at Ningbo University.

REFERENCES

ENV1993-1-3 (2006), "Eurocode 3 - design of steel structures – Part 1-3: general rules – supplementary rules for cold-formed members and sheeting", BSI.

- Hancock, G.J., Celeban M., Healy C., Georgiou P.N. and Ings N.L. (1990), "Tests of purlins with screw fastened sheeting under wind uplift", Tenth International Speciality Conference on Cold-formed Steel Structures, St. Louis, Missouri, USA.
- Katnam, K.B., van Impe R., Lagae, G. and De Strycker M (2007), "A theoretical numerical study of the rotational restraint in cold-formed steel single skin purlin-sheeting systems", *Comput. Struct.*, 85, 1185–1193.
- Katnam, K.B., van Impe R., Lagae, G. and De Strycker M (2007), "Modelling of cold-formed steel sandwich purlin-sheeting systems to estimate the rotational restraint", *Thin Walled Struct.*, 45, 584–590.
- Li, L.Y. (2004), "Lateral-torsional buckling of cold-formed zed-purlins partial-laterally restrained by metal sheeting", *Thin Walled Struct.*, 42(7), 995–1011.
- Li, L.Y. and Chu, X.T. (2007), Cold-formed steel sections, In: Martin, L.H. and Purkiss, J.A. editors. *Structural design of steelwork*. Oxford: Elsevier, 411–457. Chapter 11.
- Li, L.Y. (2010), "Calculation of moment capacity of cold-formed steel members", *Int. J. of Struct. Eng.*, 2(2), 101–115.
- Li, L.Y., Ren, C. and Yang, J. (2012), "Theoretical analysis of partially restrained zed-purlin beams subjected to up-lift loads", *J Constr. Steel Res.*, 70, 273–279.
- Lucas, R.M., Al-Bermani, G.A. and Kitiporchai, S. (1997), "Modelling of cold-formed purlin- sheeting systems - Part 1: full model", *Thin Walled Struct.*, 27(3), 223–243.
- Lucas, R.M., Al-Bermani, G.A. and Kitiporchai, S. (1997), "Modelling of cold-formed purlin- sheeting systems - Part 2: simplified model", *Thin Walled Struct.*, 27(4), 263–286.
- Peköz, T. and Soroushian, P. (1982), Behaviour of C and Z-purlins under wind uplift. Sixth International Specialty Conference on Cold-formed Steel Structures, St. Louis, Missouri, USA.
- Ren, C., Li, L.Y. and Yang, J. (2012), "Bending analysis of partially restrained channel-section purlins subjected to up-lift loads", *J. Constr. Steel Res.*, (in press).
- Rhodes, J. and Lawson, R.M. (1992), "Design of Structures Using Cold-formed Steel Sections", SCI Publication, 089, The Steel Construction Institute.
- Roger, C.A. and Schuster, R.M. (1997), "Flange/web distortional buckling of cold-formed steel sections in bending", *Thin Walled Struct.*, 27(1), 13–29.
- Rousch, C.J. and Hancock, G.J. (1997), "Comparison of tests of bridged and unbridged purlins with a nonlinear analysis model", *J. Constr. Steel Res.*, 41(2/3), 197–220.
- Sokol, L. (1996), "Stability of cold formed purlins braced by steel sheeting", *Thin Walled Struct.*, 25(4), 247–268.
- Svensson, S. E. (1985), "Lateral buckling of beams analysed as elastically supported columns subject to a varying axial force", *J. Constr. Steel Res.*, 5, 179–193.
- Toma, T., and Wittemann, K. (1994), "Design of cold-formed purlins and rails restrained by sheeting", *J. Constr. Steel Res.*, 31, 149–168.
- Vrany, T. (2006), "Effect of loading on the rotational restraint of cold-formed purlins", *Thin-Walled Struct.*, 44(12), 1287-1292.
- Vieira, Jr LCM, Malite, M. and Schafer, B.W. (2010), "Simplified models for cross-section stress demands on C-section purlins in uplift", *Thin Walled Struct.*, 48, 33–41.
- Ye, Z.M., Kettle, R., Li, L.Y. (2004), "Analysis of cold-formed zed-purlins partially restrained by steel sheeting", *Comput. Struct.*, 82, 731–739.

Ye, Z.M., Kettle, R., Li, L.Y. and Schafer, B. (2002), "Buckling behaviour of cold-formed zed- purlins partially restrained by steel sheeting", *Thin Walled Struct.*, 40, 853–864.

Table 1 Comparison of critical buckling loads and plastic failure loads.

<i>L</i> (mm)	<i>k</i> = 0		<i>k</i> = 300 N/rad		<i>k</i> = 750 N/rad	
	Failure load (kN/m)	Buckling load (kN/m)	Failure load (kN/m)	Buckling load (kN/m)	Failure load (kN/m)	Buckling load (kN/m)
4000	0.910	0.933	1.65	2.80	2.01	3.52
7000	0.280	0.130	0.533	0.722	0.676	0.935
10000	0.141	0.042	0.250	0.324	0.331	0.420

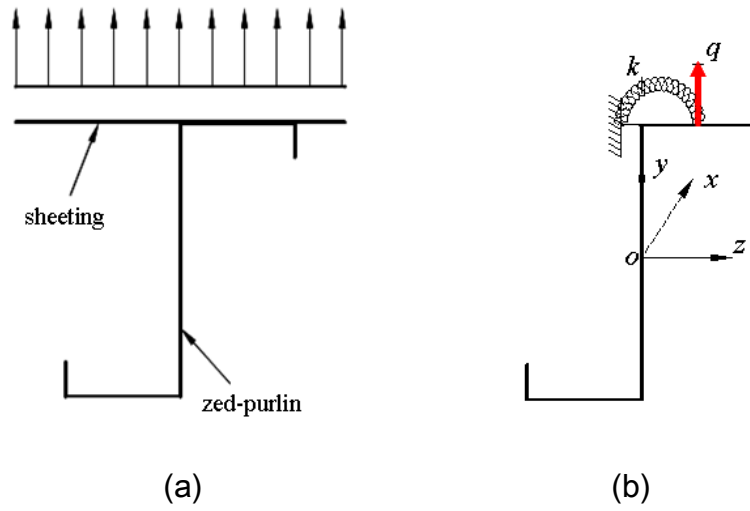
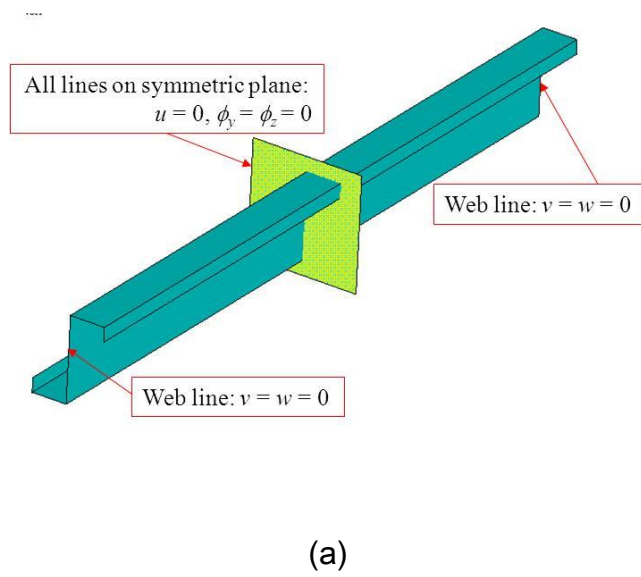
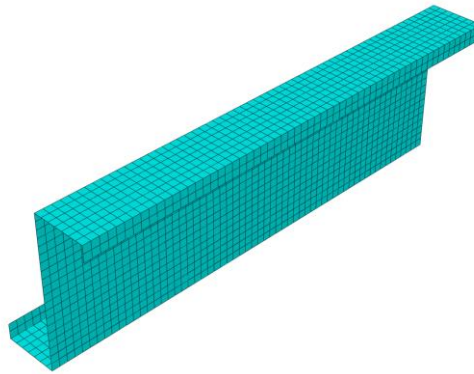


Fig.1 (a) Purlin-sheeting system and (b) the analysis model used.





(b)

Fig.2 (a) Boundary conditions used in the analyses and (b) FE mesh of a half beam model ($L/2 = 2000$ mm).

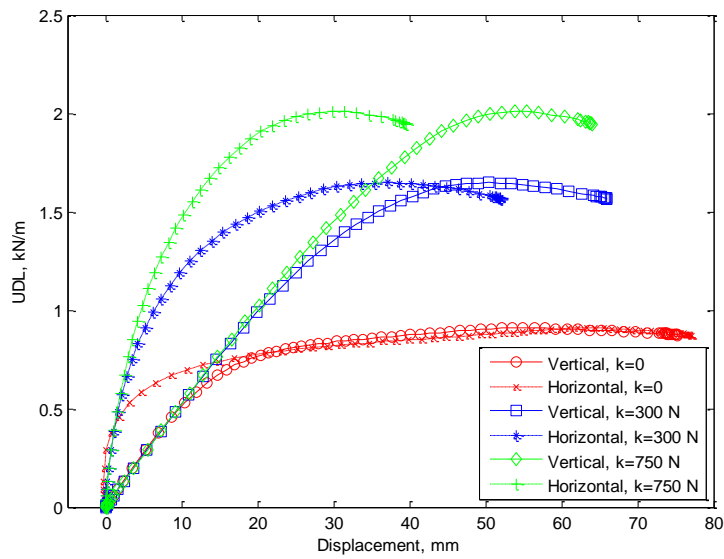


Fig.3 Load-displacement curve of purlin with different rotational spring constants ($L=4000$ mm).

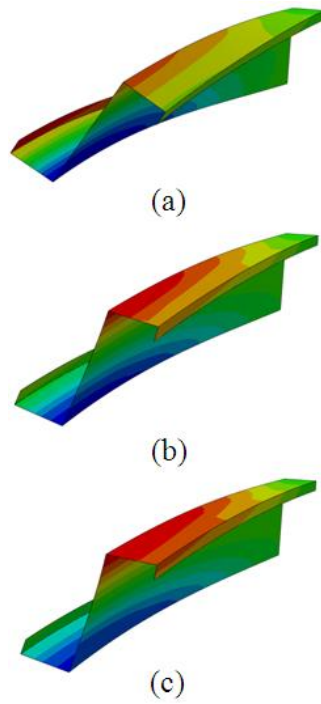


Fig.4 Deformed shape of purlin at failure point with longitudinal stress contour ($L = 4000$ mm). (a) $k = 0$, (b) $k = 300$ N/rad, and (c) $k = 750$ N/rad.

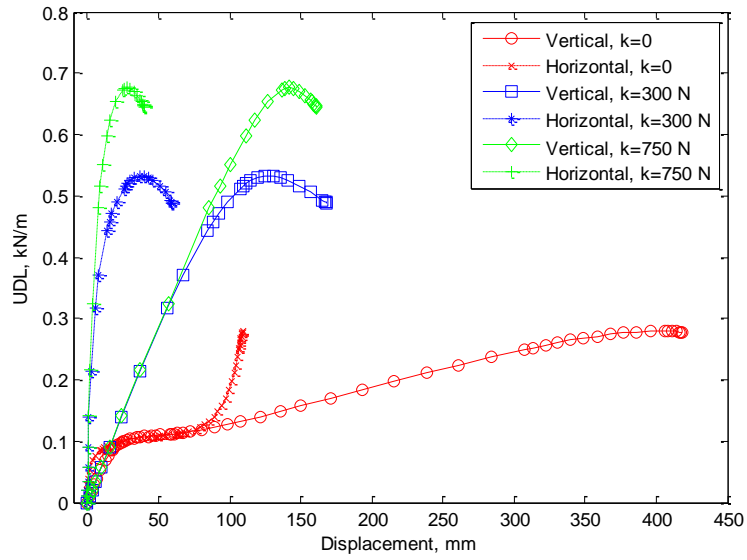


Fig.5 Load-displacement curve of purlin with different rotational spring constants ($L=7000$ mm).

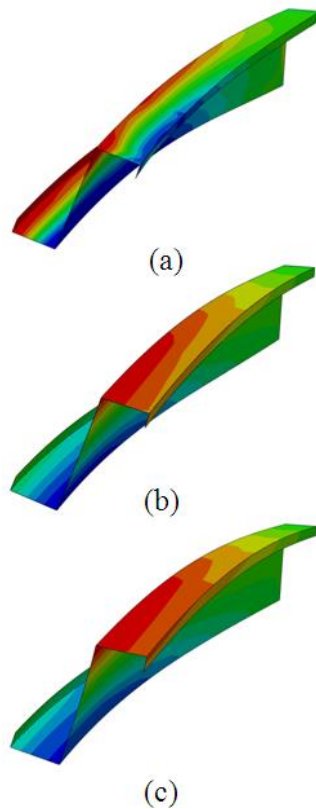


Fig.6 Deformed shape of purlin at failure point with longitudinal stress contour ($L = 7000$ mm). (a) $k = 0$, (b) $k = 300$ N/rad, and (c) $k = 750$ N/rad.

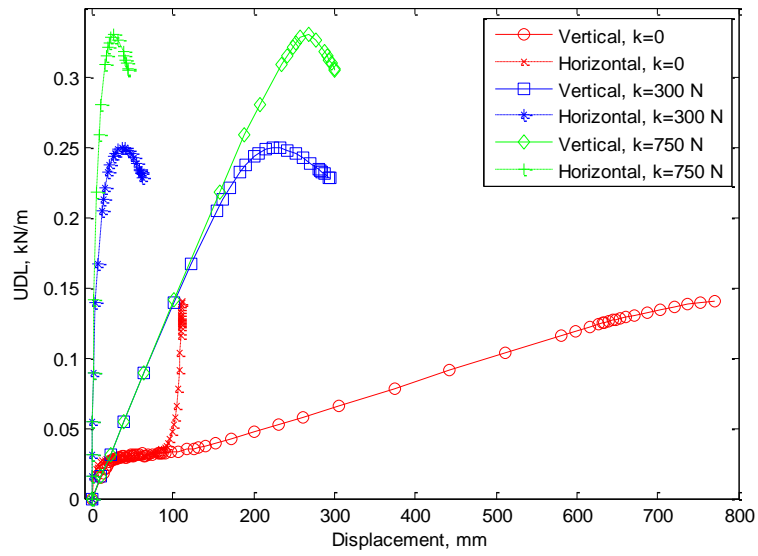


Fig.7 Load-displacement curve of purlin with different rotational spring constants

($L=10000$ mm).

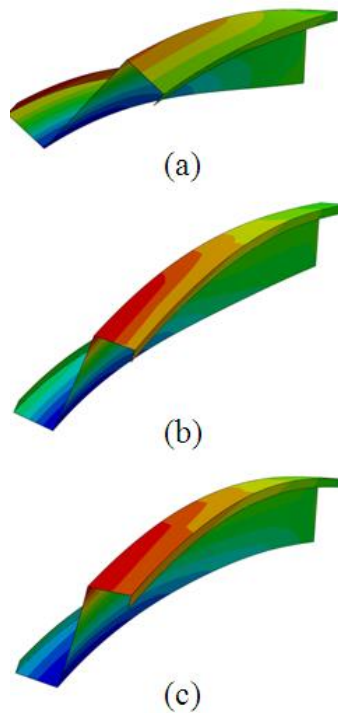


Fig.8 Deformed shape of purlin at failure point with longitudinal stress contour ($L =$

10000 mm). (a) $k = 0$, (b) $k = 300$ N/rad, and (c) $k = 750$ N/rad.

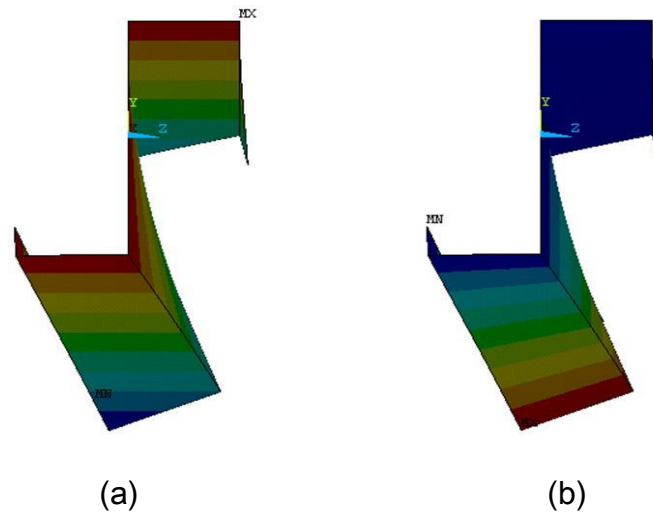


Fig.9 Initial geometric imperfection used in analysis. (a) Vertical displacement contour and (b) lateral displacement contour ($L = 4000$ mm, $k = 300$ N/rad).

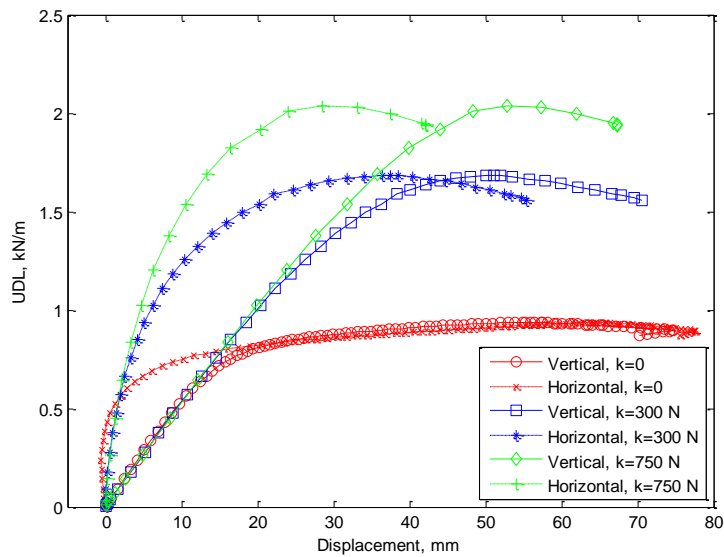


Fig.10 Load-displacement curve of imperfection purlin with different rotational spring constants ($L = 4000$ mm).

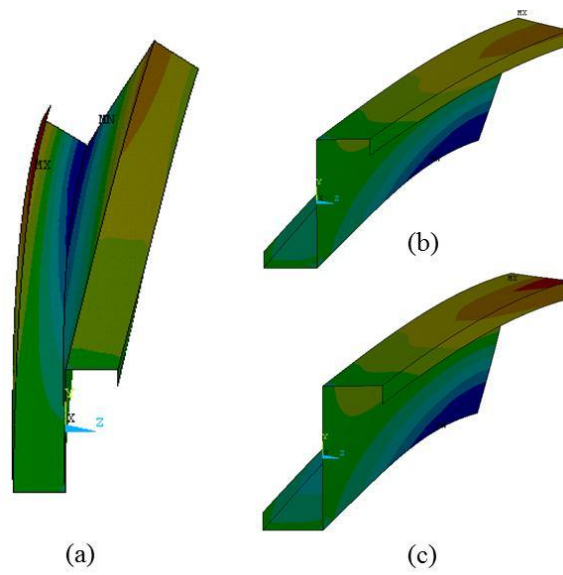


Fig.11 Deformed shape of imperfection purlin at failure point with longitudinal stress contour ($L = 4000$ mm). (a) $k = 0$, (b) $k = 300$ N/rad, and (c) $k = 750$ N/rad.

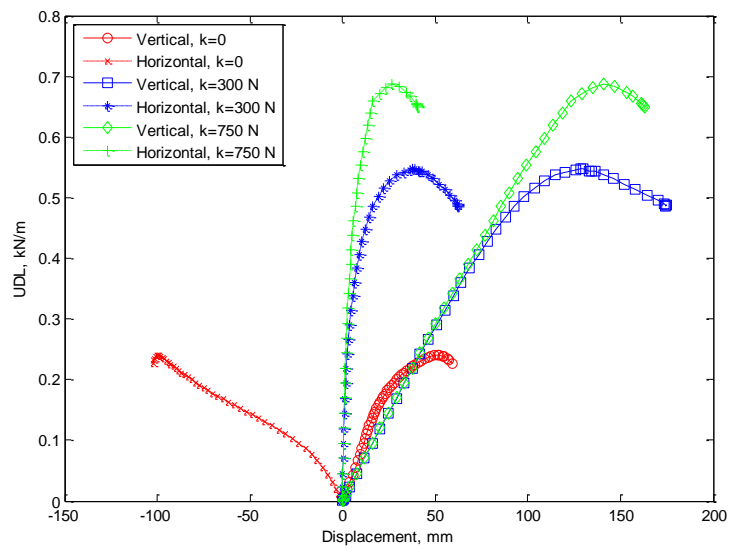


Fig.12 Load-displacement curve of imperfection purlin with different rotational spring constants ($L = 7000$ mm).

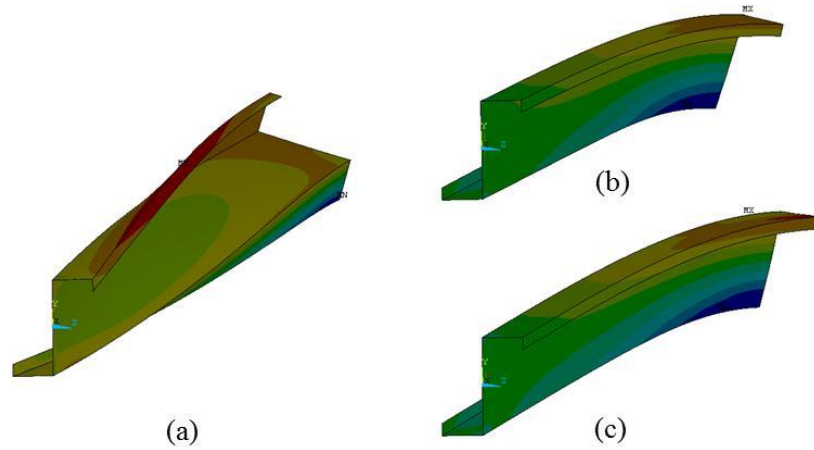


Fig.13 Deformed shape of imperfection purlin at failure point with longitudinal stress contour ($L = 7000$ mm). (a) $k = 0$, (b) $k = 300$ N/rad, and (c) $k = 750$ N/rad.

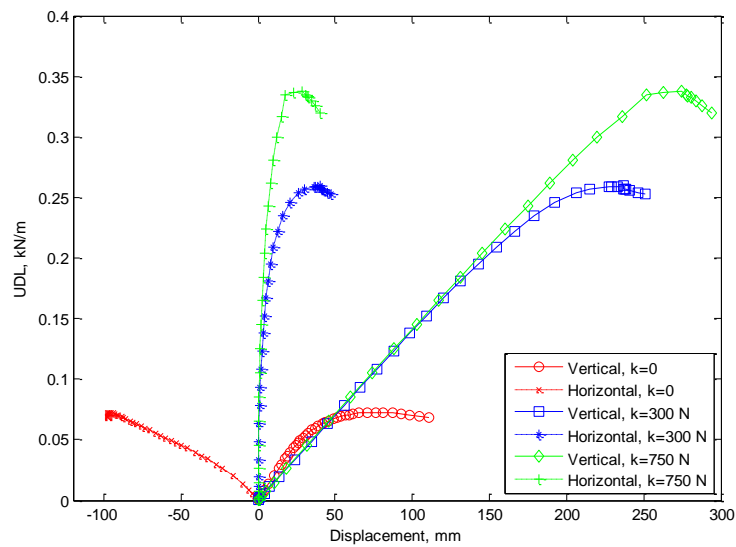


Fig.14 Load-displacement curve of imperfection purlin with different rotational spring constants ($L = 10000$ mm).

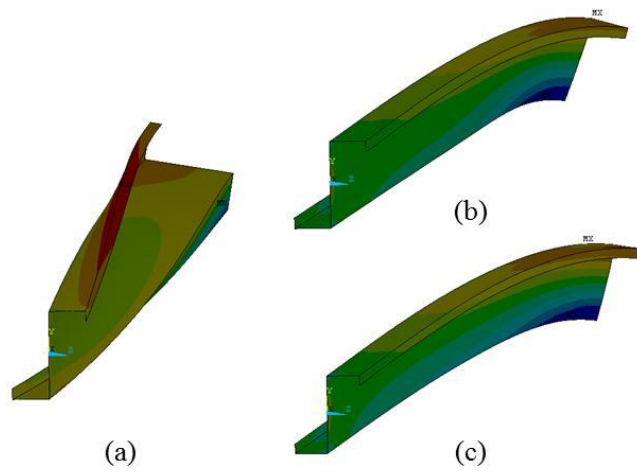


Fig.15 Deformed shape of imperfection purlin at failure point with longitudinal stress contour ($L = 10000$ mm). (a) $k = 0$, (b) $k = 300$ N/rad, and (c) $k = 750$ N/rad.

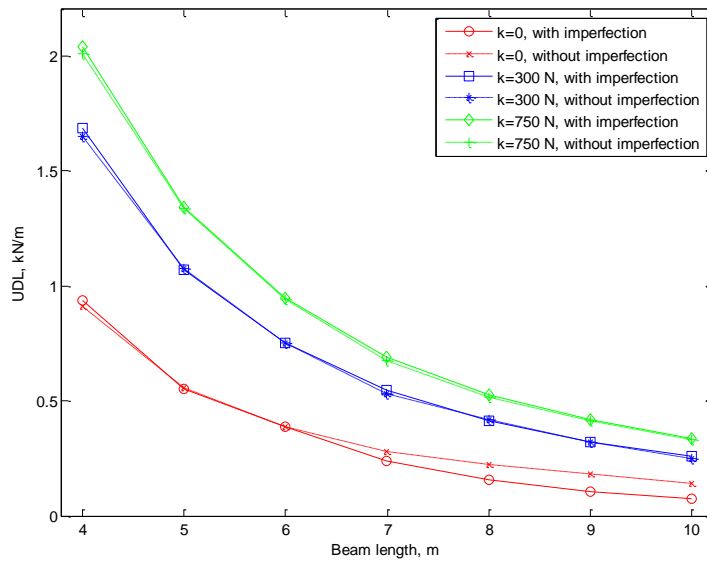


Fig.16 Variation of failure load of purlin with its length.

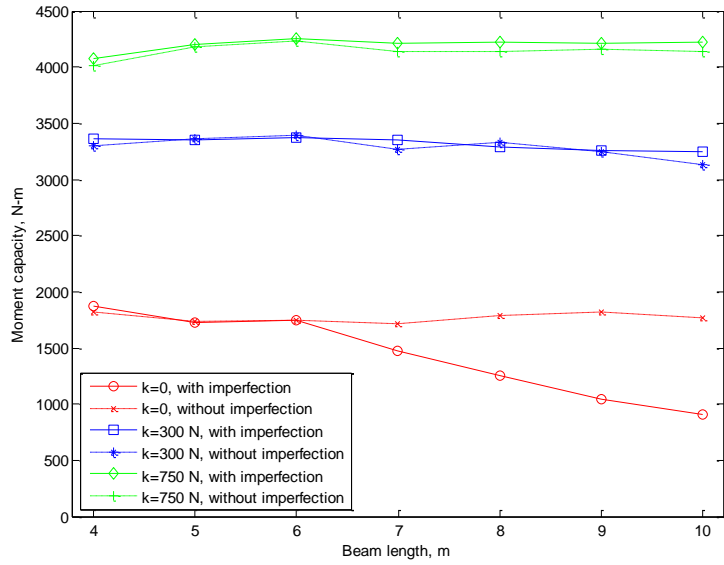


Fig.17 Variation of failure moment of purlin with its length.

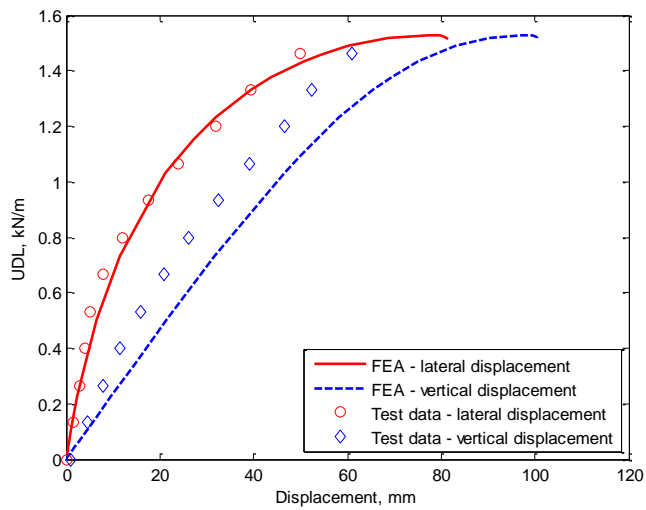


Fig.18 Comparison of FEA results with experimental data.